

Scaling Analysis of Surfactant Templated Polyacrylamide Gel Surfaces

Mukundan Chakrapani¹, S. J. Mitchell^{1,2}, D. H. Van Winkle¹, and P. A. Rikvold^{1,2}

¹*Center for Materials Research and Technology and Department of Physics,
Florida State University, Tallahassee, Florida 32306-4351*

²*School of Computational Science and Information Technology,
Florida State University, Tallahassee, Florida 32306-4120*

(Dated: November 18, 2018)

Surfaces of surfactant-templated polyacrylamide hydrogels were imaged by atomic force microscopy (AFM), and the surface morphology was studied by numerical scaling analysis. The templated gels were formed by polymerizing acrylamide plus a cross-linker in the presence of surfactants, which were then removed by soaking in distilled water. Gels formed in the presence of over 20% surfactant (by weight) formed clear, but became opaque upon removal of the surfactants. Untemplated gels formed and remained clear. The surface morphology of the gels was studied by several one- and two-dimensional numerical scaling methods. The surfaces were found to be self-affine on short length scales, with a roughness (Hurst) exponent in the range 0.85 to 1, crossing over to a constant root-mean-square surface width on long scales. Both the crossover length between these two regimes and the saturation value of the surface width increased significantly with increasing surfactant concentration, coincident with the increase in opacity. We propose that the changes in the surface morphology are due to a percolation transition in the system of voids formed upon removal of the surfactants from the bulk.

PACS numbers: 82.70.Gg, 68.37.Ps, 61.43.Hv, 05.40.-a

I. INTRODUCTION

Polyacrylamide (PAAm) gels are used extensively for separations of biological macro-molecules. Because of their intrinsically broad distribution of pore sizes they are very useful for a wide range of separations for protein isolation and sequencing of single-stranded DNA [1]. In particular, protein separations achieved by electrophoresis on gels templated with surfactant micelles have recently been reported [2], and the possibility of improvements of the separation properties, when pores of a particular size are templated within the gels, have been proposed [3]. Extensive work has also been done on the possibility of using such templated gel matrices in gel permeation chromatography (GPC) [4].

Since its introduction in 1986 [5], atomic force microscopy (AFM) has been widely used for recording images of many surfaces with resolution at small length scales. Recent developments in AFM technology have enabled its use, not only in high-resolution profiling of surface morphology and nanostructure, but also in determining local mechanical properties and in surface compositional mapping of heterogeneous samples. These applications have been extensively discussed by Magonov *et al.* [6, 7]. Despite such developments, there have been only a few reports in the literature on the direct observation of polymer gel surfaces by AFM [8, 9, 10]. Here, an AFM study of the surface morphologies of templated PAAm hydrogels and their scaling properties are presented.

We use micelles of tetradecyltrimethyl ammonium bromide (TTAB) surfactant to template pores in PAAm. Aqueous solutions of surfactant, acrylamide, and N',N'-methylene bisacrylamide (cross-linker) are mixed at various concentrations that allow the surfactant molecules to self-assemble into micelles. The solutions are then polymerized, after which the surfactants are removed by soaking in distilled water to produce templated hydrogels. A schematic representation of the templating process is shown in Fig. 1. In previous applications of TTAB templated PAAm gels for GPC [4], mean pore sizes, exclusion limits, and mechanical integrity were determined. It was shown that templated gels yield improved resolution for the separation of globular proteins from 10,000 to 150,000 Da molecular weight. Electrophoretic separations achieved on templated PAAm were also shown to be consistent with the pore-size distributions observed by GPC analysis. Templated PAAm gel matrices have the potential to improve separation efficiency over a wide range of globular protein sizes.

In this paper we present a quantitative study of the structural changes due to the templating process, using scaling analysis of AFM images of the surfaces of templated and untemplated gels. A wide variety of image-analysis tools are available with the Digital Instruments AFM software [11]. However, these are not well suited for scaling analysis of soft surfaces. Hence, we investigated the surface structure over a wide range of TTAB concentrations using our own, custom-designed surface-analysis software. This scaling analysis appears to be a robust tool to analyze and characterize surfaces imaged by AFM.

The rest of this paper is organized as follows. In Sec. II we describe the experimental procedure, apparatus, and results. In Sec. III we discuss the scaling-analysis methods. This section is subdivided into two-dimensional (Sec. III A) and one-dimensional (Sec. III B) methods. In Sec. IV we discuss the results of the scaling analysis of the AFM images,

and in Sec. V we present our conclusions.

II. EXPERIMENTAL

PAAm gels were formed at room temperature by free-radical polymerization with chemical initiators from a mixture of monomer, cross-linker, buffer, and surfactant. The gels were cast between two glass slides separated by 1.5 mm spacers. The glass slides were ordinary pre-cleaned microscope slides (Fisher Scientific). They were cleaned with detergent and rinsed in distilled water and air dried before use. AFM images (not shown here) of these slides revealed a root-mean-square (rms) roughness of less than a nanometer over several square micrometers. Acrylamide (Electrophoresis Grade, Fisher Scientific) solutions were polymerized in the presence of a TBE buffer (45 mM tris-borate, 1 mM EDTA) at pH 8.3. The chemical initiators were ammonium persulfate (Ammonium Peroxydisulfate, Certified A.C.S., Fisher Scientific) and N, N, N', N'-tetramethylethylenediamine (TEMED, Fisher Scientific). The concentration of acrylamide was kept constant at 40% by weight, and that of the cross-linker, N',N'-methylene bisacrylamide (Bis-acrylamide, Electrophoresis Grade, Fisher Scientific) was held at 7% of the acrylamide concentration in all samples. Various amounts of the surfactant, TTAB (Sigma-Aldrich), were added to form the templated gels. The amount of surfactant added was so that the final surfactant concentration ranged from 0% to 40% by weight in steps of 10%. The presence of surfactant micelles did not prevent the formation of PAAm gels. The rates of polymerization were, however, altered by the presence of surfactants. Higher concentration of surfactants in the pre-gel solution reduced the rate of acrylamide polymerization. All pre-gel solutions were clear, homogeneous solutions with viscosities dependent on the amount of surfactant. The resulting templated gels were all optically clear before surfactant removal.

After polymerization, the gels were peeled off the glass plates and soaked in distilled water to remove the surfactants by diffusion. More than 98% of the surfactants diffused out of the gel upon soaking for about two days. Several methods, including Raman spectroscopy have been used to quantify the removal of the surfactant templates by free diffusion into water [4]. During the surfactant-removal process, gels with surfactant concentrations of more than 20% transformed into white homogeneous materials. This suggests a structural change in the templated gels, involving a length scale comparable to the wavelength of visible light. This further indicates that the structural change is associated with kinetic restructuring of the gel during and after the removal of micelles.

The gel surfaces were imaged using AFM (Digital Instruments, D3000) with a silicon nitride probe (Digital Instruments) of spring constant 0.32 N/m. Scans were performed in contact mode under water (HPLC grade). The set-point voltage was kept at the lowest possible value to minimize the risk of damage to the gel. The inherent soft nature of the gels under investigation can cause difficulties in imaging and affect the reproducibility of the images. In order to overcome this difficulty, we devised a sample holder which helped provide the required stability and hence improved the reproducibility of the images. This sample holder consists of a stainless-steel block with a well in the center, into which the sample is placed. The sample is then covered using a thin steel cover slip with a hole in the center for imaging. The cover slip is held in place with mounting screws (see Fig. 2).

After the surfactants were removed by soaking, three different locations on each gel surface were selected for imaging, and a set of centered, zoomed images were obtained for each location. The image sets were created by scanning the surface from small scan sizes up to larger sizes, in sequence. The images were all $L \times L$ squares with sides $L=1.25, 2.5, 5.0, 10.0,$ and $20.0 \mu\text{m}$, respectively. This process yielded a set of successively zoomed-out images of the same location. The lateral drift of the sample was very small. Figure 3 shows one such zoomed set, and the excellent reproducibility of the images justifies the use of the cover slip holder. To further test the reproducibility, drift, and surface distortion, two images were obtained for each scan size, first in the forward scanning direction, and next in the reverse scanning direction, before changing to the next scan size (see Fig. 4). Some distortion along the direction of the tip motion is noticeable. All images have 512×512 pixel resolution, regardless of scan size, and all imaging was performed at room temperature.

This telescoping scanning procedure produced a set of ten images for each location and a total of thirty images for each gel. With this procedure, five different gels were examined with surfactant concentrations of 0, 10, 20, 30, and 40%, yielding a total set of 150 images (75 forward scans and 75 reverse scans). Many of the images were too noisy for analysis, and all 150 images were examined for quality in a blind procedure in which two of the authors, who had not themselves acquired the data, were separately shown all 150 images. They indicated whether each image should be retained for analysis. If an image was indicated as too noisy by either individual, that image was excluded from analysis. This procedure yielded a total of 106 images for analysis, as detailed in Table I.

The gel surfaces were also imaged using tapping mode under water. A single set of ten images as described above was obtained for gels with surfactant concentrations of 0% and 40%. The surface morphologies were statistically indistinguishable from those obtained using contact mode. Since tapping mode is rather time consuming and did not provide any apparent advantage over contact mode, all the data presented here were collected in contact mode.

Figure 5 shows examples of AFM images ($L = 10.0 \mu\text{m}$) of gel surfaces with each of the five different template

concentrations. The gels exhibit marked statistical differences, most notably that the height range of the surface depends on both the surfactant concentration and the length scale of the scan. This is clearly seen in the three-dimensional visualizations of the gel surface, shown in Fig. 6. Typical scan lines for gel surfaces at various surfactant concentrations are shown in Fig. 7. On the 10 μm length scale, the untemplated gels have height ranges on the order of a few nanometers, while the 40% templated gels have height ranges on the order of a few hundred nanometers. AFM images and Raman spectroscopy of glass plates before and after polymerization and gel removal indicated that there was no polymer left behind on the glass. This suggests that the gel surfaces imaged by AFM are relaxed, free surfaces, rather than fracture surfaces.

The surface analysis routines available with the D3000 only quantify changes in the overall surface width (often called “the surface roughness”). In contrast, our statistical analysis shows self-affine scaling behavior at small length scales, which crosses over to a length-scale independent behavior at large length scales, as discussed in Sec IV. As we are interested in the behavior of the surface on a wide range of length scales, no image filtering or processing was performed, with the exception of flattening (described in Sec. III A). It is our opinion that scaling analysis of filtered images could be highly suspect since the essence of most image processing techniques is to alter the data differently on different length scales. All analysis was performed with our own code, written in C, as discussed in Sec. III.

III. ANALYSIS METHODS

We here present a well-defined procedure to characterize surfaces, based on the statistical analysis methods described in Refs. [12, 13]. One common measure of surface morphology is the rms height of the surface, which is sometimes referred to as the “rms roughness” (referred to here as the rms surface width),

$$w = \sqrt{\frac{\sum_{i=1}^{M^2} h_i^2}{M^2} - \left[\frac{\sum_{i=1}^{M^2} h_i}{M^2} \right]^2}, \quad (1)$$

where h_i is the i th value of the height in an image consisting of $M \times M$ pixels. (For all of our images, $M = 512$.) However, such a drastic simplification of the surface structure to only one single number ignores nearly all of the morphological information contained in the image. Reporting the surface width without specifying further details can be meaningless. The value of the width is highly dependent, not only on the image processing methods used [14], but also on the length scale of observation [15]. We therefore present a comprehensive scaling analysis of the gel surfaces which goes beyond the simple single w description.

The surface width defined by Eq. (1) for a $L \times L$ (μm^2) image of $M \times M$ pixels varies with L . For a variety of different surfaces the width is found to exhibit different length dependences with two limits:

$$w \propto \begin{cases} L^\alpha & L \ll l_\times \\ w_{\text{sat}} & L \gg l_\times \end{cases}, \quad (2)$$

where the exponent α is the Hurst exponent (in this study equal to the roughness exponent [16]), w_{sat} is a constant saturated surface width, and l_\times is a cross-over length scale between the two behaviors. In general, α , l_\times , and w_{sat} depend on the details of the surface, such as the surfactant concentration in the present study.

The power law in Eq. (2) is a consequence of self-affine scaling behavior, in which the surface is statistically invariant under the transformation [12]

$$x \rightarrow bx, \quad y \rightarrow by, \quad h \rightarrow b^\alpha h, \quad (3)$$

where x and y are distances in the two image-scan directions, h is the height, and b is a dimensionless re-scaling factor. Self-affine behavior is different from self-similar behavior, which involves invariance under the isotropic scale-change transformation [12] $x \rightarrow bx$, $y \rightarrow by$, and $h \rightarrow bh$. This distinction between self-affine and self-similar structures is often overlooked, and the term “fractal” is used somewhat freely for both in the literature.

If the surface were ideally self-affine, then the power-law behavior in Eq. (2) would continue on all length scales, and there would be neither a saturation width, w_{sat} , nor any identifiable length scale such as l_\times or a typical feature size. For a surface whose heights are described by an ideal random walk, $\alpha = 1/2$ and $l_\times \rightarrow \infty$. For most surfaces, measured values of α are between 1/2 and 1 [17, 18, 19], even for such different surfaces as brittle rocks ($\alpha \approx 0.78$) [20] and CuCl islands on CaF_2 ($\alpha \approx 0.84$) [21]. As discussed in Sec. IV, our estimates of α for the different gel surfaces all fall within the range [0.5, 1.0], and w_{sat} and l_\times vary strongly with the surfactant concentration.

In the following subsections, we discuss several different methods used to examine the scaling behavior of the gel surfaces. Both two-dimensional analysis methods that analyze the image as a whole, and one-dimensional methods that analyze the image one scan line at a time were examined.

A. Two-Dimensional Methods

The AFM records the vertical surface height, $h(x, y)$, as a function of the fast (x) and slow (y) scanning directions. As already discussed, L dependent surface widths can be obtained from $L \times L$ (μm^2) images. After imaging at a sufficiently large number of scan sizes (different L 's), α , w_{sat} , and l_x can be obtained. However, the number of images required for such an analysis is large. By noting that each image contains information about length scales from L/M (where M is the number of pixels) up to L , one can perform analyses over a wide range of length scales from a single AFM image. Several variations of two-dimensional analysis methods were studied. We discuss a spectral method based on the Fourier transform of the image [13], a box-counting method from subsections of images, and widths calculated from the same subsections of the image [12]. All of the images were flattened using the AFM software [11] and not processed any further. The flattening procedure fits a straight line to each scan line by the method of least squares, which is then subtracted from the data. The fitting and subtracting procedure was applied, independently, to each scan line in the image. After flattening, the average height and slope in the x -direction (the fast scan direction) are zero.

For the spectral methods, we computed the structure factor, $S(\vec{k}) \propto |\mathcal{F}_{\vec{k}}(h(x, y))|^2$, which is the absolute square magnitude of the complex Fourier transform of the surface height. Here, \vec{k} is the wave vector in the x, y plane. For large k , the structure factor should scale as $S(k) \propto k^{-(2+2\alpha)}$ [13], a generalized Porod's Law [22]. The presence of anisotropy in the AFM images produces ridges along the k_x and k_y directions as shown in Fig. 8. This made circular averaging unreliable, and hence the results from spectral methods were suspicious. The presence of the ridges seems to be a general feature of AFM imaging, as has been observed for hard materials as well [14]. Removal of these ridges (which have a non-zero width) by a technique such as that suggested in Ref. [14] would require *a priori* knowledge of their functional form.

For both the box-counting and width methods, the $L \times L$ (μm^2) image of $M \times M$ height values (pixels) was recursively subdivided into non-overlapping images of $l \times l$ (μm^2) with $(M/n) \times (M/n)$ pixels, where $l = L/n$ μm and $n \leq M/2$ is an integer denoting the level of subdivision. For each value of l , $(L/l)^2$ different sub-images were obtained. Non overlapping sub-images were used to ensure statistical independence.

A box-counting method was tried following Ref. [12]. The minimum number of cubic boxes of side l needed to span the height range of a sub-image of $l \times l$ μm^2 was calculated. However, the height range was nearly always less than l , yielding the total number of boxes to be one, regardless of the length scale. This would seem to imply $\alpha = 1$. Thus the box-counting method is entirely insensitive to the scaling behavior of the gel surfaces.

The rms width for the j -th sub-image of size $l \times l$,

$$w_{lj} = \sqrt{\frac{\sum_{i=1}^{(M/n)^2} h_i^2}{(M/n)^2} - \left[\frac{\sum_{i=1}^{(M/n)^2} h_i}{(M/n)^2} \right]^2}, \quad (4)$$

and its average, $\langle w_l \rangle$, over all sub-images of size l were calculated. Typical results are shown in Fig. 9. For a discussion of the effects of changing the order of the averaging and the square root, see Ref. [23].

Among the several two-dimensional analysis methods used to study the scaling properties of the gel surfaces, the calculation of $\langle w_l \rangle$ was found to provide the most reliable results. The other methods have inherent disadvantages as discussed in the preceding paragraphs. As we shall explore in the next subsection, the scanning process introduces noise between the scan lines, and for a more accurate analysis, one-dimensional methods should be used.

B. One-Dimensional Methods

If there is noise in the measurement process we would expect to measure $h_{\text{measured}}(x, y) = h(x, y) + h_{\text{noise}}$, where the noise adds an effective offset. If we further assume that h_{noise} is a random walk in time, noise correlations in time would appear as correlations in space. Furthermore, if the noise varies sufficiently fast compared to the scanning velocity, h_{noise} at the beginning of each scan line will be completely uncorrelated. Thus for a perfectly flat surface with $h(x, y) = 0$, each scan line would appear to be a random walk with $\alpha = 1/2$, with little or no correlation between scan lines. Motivated by these considerations and the extremely small height ranges in the gels with 0% and 10% surfactant, we constructed a one-dimensional analysis procedure which analyzes the images one scan line at a time, where a scan line is a line in the fast (x) scan direction.

One-dimensional surface widths $\langle w_l \rangle$ were calculated in a manner equivalent to that defined in Eq. (4) with j now representing a sub-interval in the fast scan direction instead of a sub-image and $(M/n)^2$ replaced by (M/n) . The w_{lj} , for all j and all scan lines, were then averaged to get the $\langle w_l \rangle$ for the image. The surface width calculations at the smallest image sub-interval depends strongly on the definition of w_l (see Eq. (4)). When applied to a straight line

($\alpha = 1$), the standard one-dimensional estimate of $\langle w_l \rangle$ used here overestimates α by as much as 20% for sub-intervals that contain less than four data points. The results of the one-dimensional surface width analysis are presented in Table II and in Sec. IV.

While surface-width calculations contain information about all length scales $\leq L$, calculation of correlation functions yield information at a specific value of relative separation. We define the height-height correlation function of a scan line at fixed y as

$$C(r, y) = \langle h(x, y)h(x + r, y) \rangle_x - \langle h(x, y) \rangle_x^2, \quad (5)$$

where r is a relative displacement in the x direction, and $\langle \cdot \rangle_x$ denotes an average over all values of x in the scan line. Note that after flattening, the second term is zero, and that $C(0, y)$ is the rms width of the scan line, $w(y)$. Although the flattening was necessary to compensate for non-horizontal mounting of the gel and/or gradients in the gel thickness, it introduces correlations at the length scale L . Consequently, correlation functions for flattened images are meaningful only for lengths, $l \leq L/2$. For scaling analysis, it is more convenient to deal with an alternative form of the correlation function, which is sometimes referred to as the variance of increments [24] or the increment correlation function,

$$H(r, y) = \langle |h(x + r, y) - h(x, y)|^q \rangle_x. \quad (6)$$

For the special case of $q = 2$,

$$H(r, y) = \langle [h(x + r, y) - h(x, y)]^2 \rangle_x = 2[w(y)^2 - C(r, y)]. \quad (7)$$

The correlation functions in the slow (y) scan direction, $C(x, r)$ and $H(x, r)$, can be analogously defined.

To improve the statistical accuracy of the increment correlation function measurements, multiple scan lines must be used. Thus, we define the first and second moments as

$$\begin{aligned} H_{\text{fast}}(r) &= \langle H(r, y) \rangle = \sum_{j=1}^p \left[\sum_{i=1}^M H(r, y = iL/M) \right] / pM, \\ \langle H(r, y)^2 \rangle &= \sum_{j=1}^p \left[\sum_{i=1}^M H(r, y = iL/M)^2 \right] / pM, \end{aligned} \quad (8)$$

where $\sum_{j=1}^p$ runs over the p different scan lines. The standard error of $\langle H(r, y) \rangle$ is then $\sigma_{\text{fast}} = \sigma(r, y) = \sqrt{\frac{\langle H(r, y)^2 \rangle - \langle H(r, y) \rangle^2}{pM-1}}$. Again, the moments and error in the slow scan direction can be analogously defined.

The increment correlation function for $q = 2$ is expected to scale as

$$H_{\text{fast}}(r) \propto \begin{cases} r^{2\alpha} & r \ll l_{\times} \\ 2w_{\text{sat}}^2 & r \gg l_{\times} \end{cases}. \quad (9)$$

In Fig. 10 we see power-law scaling for small r and an apparent cross-over to saturated values at large r . When the noise-induced offsets between scan lines are small, $H_{\text{slow}}(r)$ should have the same scaling as $H_{\text{fast}}(r)$. However, if the signal-to-noise ratio is small, we expect $H_{\text{slow}}(r)$ to measure only the noise with $\alpha = 1/2$. Figure 11 shows plots of $H_{\text{slow}}(r)$ and $H_{\text{fast}}(r)$ for 0% and 40% templated gel surfaces. For the untemplated gel surfaces the fluctuations due to noise in the slow scan direction are comparable to the signal. Thus $H_{\text{slow}}(r)$ does not follow $H_{\text{fast}}(r)$. For the 40% templated gel surfaces, the random offsets between scan lines are relatively smaller, but not negligible. Hence $H_{\text{slow}}(r)$ is much closer to $H_{\text{fast}}(r)$.

By evaluating the increment correlation function and plotting $H_{\text{fast}}(r)$ on a log-log scale, the roughness exponent α , the limiting surface width w_{sat} , and the lateral cross-over length l_{\times} can be determined from the slope in the small- r linear regime (see Fig. 10), the limiting value of $H_{\text{fast}}(r)$ for large r , and the inflection point of the logarithmic derivative of $H_{\text{fast}}(r)$ (see Fig. 12), respectively.

IV. RESULTS AND DISCUSSION

As shown in the previous sections, among the two-dimensional analysis methods, only the l -dependent surface width $\langle w_l \rangle$ gives meaningful results for this system. The l -dependence of this quantity was presented in Fig. 9 and is essentially similar to that of the one-dimensional surface-width (not shown) and the one-dimensional increment correlation function shown in Fig. 10. All three quantities show a self-affine scaling region on short length scales, and a saturated plateau on large length scales. These two scaling regimes are separated by the crossover length l_{\times} . Both the crossover length and the saturation value increase with increasing surfactant concentration.

The values of the roughness exponent α extracted from the self-affine regime for the surface width measurements (both two-dimensional and one-dimensional), along with those calculated from the one-dimensional increment correlation function with $q = 2$, are listed in Table II. Using $q \neq 2$ in Eq. (6) yielded the same values of α as obtained with $q = 2$. This indicates that the gel surfaces are perfectly self-affine on these short length scales, rather than multi-affine [16, 23, 25]. A plot of the estimated values of α vs the surfactant concentration is shown in Fig. 13. The estimates obtained from the two-dimensional surface width measurements and from the one-dimensional increment correlation function agree well for 20%, 30%, and 40% templated surfaces. We believe that the lack of agreement for 0% and 10% templated surfaces is associated with the low signal-to-noise ratio in the images for these gels. The vertical resolution limit of the AFM ($\gtrsim 0.1$ nm [11]) contributes to the uncertainty since the height variations are only about 1 nm for the lowest surfactant concentrations.

The values for α , determined from the one-dimensional surface-width measurements, are consistently higher than those obtained from the other two measurements. As discussed in Sec. III B, the roughness exponents obtained using the one-dimensional surface width for intervals with only a few data points are consistently too high, and this may be at least part of the explanation for the discrepancy. The values of α for 20%, 30%, and 40% templated surfaces obtained from two-dimensional surface-width and one-dimensional correlation-function measurements are clustered between 0.80 and 0.89. However, measurements of surface-roughness exponents from relatively small data sets, such as the present ones, tend to have systematic errors, as well as random ones, and the calibration curves for synthetic data sampled over 512 points, given in Ref. [26], indicate that the values obtained here may be underestimated by up to 10%. Thus, based on our results it is not unreasonable to conclude that all of these surfaces have the same roughness exponent in the range 0.85 to 1.0, irrespective of the surfactant concentration. A roughness exponent in this range is consistent with previous results for N-isopropylacrylamide gel surfaces by Suzuki *et al.* [9]. However, as discussed in the next paragraph, the *magnitude* of the height variations depends strongly on the surfactant concentration, as do the crossover length l_\times and the saturation surface width w_{sat} .

The limiting value of the surface width on large length scales, w_{sat} , is found to increase by almost two orders of magnitude as the surfactant concentration is increased from 0% to 40%. This behavior is evident from Figs. 7, 9(a), 10(a), and 14. The measurements of w_{sat} are listed in Table II and displayed vs surfactant concentration in Fig. 14. Similarly, but less spectacularly, l_\times increases by about a factor of two, as shown in Table II and Fig. 15.

As the surfactants are removed, the transparency of some of the gels change. The gels that contained no or little surfactant stay clear. On the other hand, gels that had higher concentrations of surfactant (more than 20%) become opaque and white as the surfactant diffuses out. Using the theory of light scattering by refractive index fluctuations, an expression for the spectral density of light scattered can be obtained. Reasonable functional forms for the correlation function can then be used to obtain the turbidity or inverse attenuation length. A detailed derivation is provided in the Appendix. The turbidity for a wavelength $\lambda = 550$ nm in the visible region is shown as a function of the correlation length ξ in Fig. 16. The two curves presented correspond to an isotropic exponential and Gaussian correlation function, respectively. If we associate the correlation length ξ with the saturation value of the rms surface width, w_{sat} , we notice that the turbidity increases by about six orders of magnitude as w_{sat} changes from 1 nm for the 0% templated gel to 80 nm for the 40% templated gel. These changes in the turbidity are consistent with a change from a transparent to an opaque material. Our justification for the association between ξ and w_{sat} is discussed below.

The experimental results presented here indicate that while the templated gel surfaces are self-affine on small to moderate length scales, with α in the range 0.85 to 1, both the crossover length and the saturation value of the surface width increase significantly with the bulk concentration of surfactant. From Figs. 14 and 15 it is clear that most of these increases occur only after the surfactant concentration exceeds about 20%. This indicates that the dramatic changes seen in the surface structure are reflections of a sharp transition in the bulk structure, most likely a percolation transition at which the surfactant structure changes from a spatial distribution of individual micelles to a percolating network. These different structures apparently do not seriously affect the mechanical properties of the gel as long as the surfactants are in place. However, once they are soaked out, the resulting percolating void network is likely to weaken the gel and lead to large relaxations as the elastic polymer network readjusts its configuration. While the percolation threshold is a non-universal quantity and thus depends on the particular system, for site percolation on standard three-dimensional lattices it lies roughly in the range from 20 to 30 percent by volume [27]. This is consistent with the range in which the surface structure and the opacity of the templated gels undergo their strongest changes. Previous work on the phase diagrams of alkyltrimethylammonium surfactants [28] suggests a transition from micelle to hexagonal phase at around 35 wt% TTAB at room temperature.

Further support for the percolation hypothesis is provided by recent computer simulations of a two-dimensional frustrated spring network with a free surface and a variable density of holes [23, 29], which were inspired by the experimental results presented here. In those simulations the structure of the free surface remains relatively constant, with a self-affine structure on short length scales and a finite saturation width on large length scales, as long as the volume fraction of holes is far below the percolation limit. As the hole concentration approaches the percolation threshold, both the the saturation width and the crossover length increase in a manner qualitatively similar to our

experimental observations. The saturation width, in particular, appears to follow the same power-law divergence as the bulk correlation length over a wide range of hole concentrations approaching the percolation threshold. These observations form our justification for the association of w_{sat} with the bulk correlation length in the estimate of the change in the turbidity, discussed above.

V. CONCLUSION

We have obtained AFM images of relaxed, free surfaces of PAAm hydrogels templated with TTAB surfactant and performed a numerical scaling analysis of the observed surface structure. In doing so, we have developed methods that can be used not only for our data, but also to perform scaling analysis of any surface imaged by an AFM. We showed that the calculation of the two-dimensional surface width and one-dimensional correlation functions gave consistent, useful results. Two-dimensional box-counting and spectral methods were unsatisfactory, while results from one-dimensional surface-width measurements provided over-estimates at small length scales. The one-dimensional increment correlation function in the fast scan direction, $H_{\text{fast}}(r)$, is simple to calculate and gives a reliable characterization of rough surfaces. By calculating this correlation function we have determined that the surfaces of the templated gels are self-affine over a significant range of small and intermediate length scales, with a roughness (Hurst) exponent in the range 0.85 to 1. This self-affine regime is terminated by a cross-over length, above which the surface width is scale independent. The increases in the cross-over length and the saturation width of the surface with increasing surfactant concentration coincides with the observation of a large increase in the scattering of visible light. We propose that the observed effects are caused by a percolation transition in the bulk surfactant system, from isolated micelles to a percolating network. Further investigations of the bulk structure of the gels at different surfactant concentrations are planned.

Acknowledgments

We thank R. L. Rill, G. M. Buendía, P. Meakin, and S. Hong for useful discussions, and E. Lochner for his assistance with the AFM and the development of the new sample holder. G. Brown, K. Park, and S. Wang are acknowledged for their comments on the manuscript. We thank B. van de Burgt for the Raman spectroscopy results and analysis, and A. Beheshti is acknowledged for his help in testing the validity of our data-analysis code. Supported in part by NSF grants No. BES-951381 and DMR-9981815, and by Florida State University through the Center for Materials Research and Technology and the School of Computational Science and Information Technology.

APPENDIX A

The theory of light scattering by refractive-index fluctuations leads, in the Born approximation, to the following expression for the spectral density of light scattered from a volume V , a distance R away in the far-field zone [30]:

$$I(\vec{k}) = I_0 \frac{V}{R^2} \frac{(2\pi)^4 \sin^2 \psi}{2\lambda^4} \mathcal{S}^{(\delta n)}(\vec{k}), \quad (\text{A1})$$

where

$$\mathcal{S}^{(\delta n)}(\vec{k}) = \int_V d^3r G(\vec{r}) \exp[i\vec{k} \cdot \vec{r}]. \quad (\text{A2})$$

Here I_0 is the intensity of the incident light, λ is the wavelength of the scattered light, ψ is the polarization angle, \vec{k} is the scattering wave vector, and $G(\vec{r}) = \langle \delta n(\vec{r}_0) \delta n(\vec{r}_0 + \vec{r}) \rangle / \langle (\delta n)^2 \rangle$ is the normalized correlation function for the refractive-index fluctuations $\delta n = n - \langle n \rangle$.

We can calculate the total scattering intensity at a particular wavelength λ by using the relation $|\vec{k}| = \frac{4\pi}{\lambda} \sin(\frac{\theta}{2})$, where θ is the scattering angle, and integrating $I(\vec{k})$ over all angles, *i.e.*,

$$I(\lambda) = I_0 \frac{V}{R^2} \Lambda^{-1}(\lambda, \xi) \quad (\text{A3})$$

where the turbidity or inverse attenuation length is

$$\Lambda^{-1}(\lambda, \xi) = \int d\theta d\phi \sin \theta \frac{1}{2} (1 + \cos^2 \theta) \mathcal{S}^{(\delta n)}(\vec{k}), \quad (\text{A4})$$

and ξ is the bulk correlation length. The term in the integral of the form $(1 + \cos^2 \theta)/2$ corresponds to unpolarized incident light [31]. Assuming an isotropic exponential correlation function, $G(r) = \exp[-r/\xi]$, we find

$$\Lambda^{-1}(\lambda, \xi) = \frac{4\pi^3 \langle (\delta n)^2 \rangle}{\lambda} \frac{a^2 + 2}{a} \left[\frac{a^2 + 2}{a^2 + 1} - \frac{2 \ln(a^2 + 1)}{a^2} \right], \quad (\text{A5})$$

where $a = 4\pi\xi/\lambda$. Alternatively, using a Gaussian correlation function, $G(r) = \exp[-(r/\xi)^2]$, we find

$$\Lambda^{-1}(\lambda, \xi) = \frac{2\pi^{7/2} \langle (\delta n)^2 \rangle}{\lambda a^3} \left\{ (64 - 8a^2 + a^4) - (64 + 8a^2 + a^4) \exp[-a^2/4] \right\}. \quad (\text{A6})$$

A reasonable value for the mean refractive-index fluctuation between the PAAm and water regions in a gel is $\langle (\delta n)^2 \rangle = 0.01$. The resulting turbidity, as given by Eqs. (A5) and (A6), is shown in Fig. 16.

-
- [1] M. Chiari and P. G. Righetti, *Electrophoresis* **16**, 1815 (1995).
 - [2] R. L. Rill, B. R. Locke, Y. Liu, J. Dharia, and D. H. Van Winkle, *Electrophoresis* **17**, 1304 (1996).
 - [3] R. L. Rill, B. R. Locke, and D. H. Van Winkle, *Anal. Chem.* **70**, 13 (1998).
 - [4] B. C. Patterson, *Surfactant micelles as templates in hydrogels*, Ph.D. dissertation. (Florida State University, Tallahassee, 2000).
 - [5] G. Binnig, C. F. Quate, and C. Gerber, *Phys. Rev. Lett.* **56**, 930 (1986).
 - [6] S. Magonov and D. Reneker, *Ann. Rev. Mater. Sci.* **27**, 175 (1997).
 - [7] S. Magonov and M. Heaton, *American Laboratory* **30**, 10 (1998).
 - [8] A. Suzuki, M. Yamazaki, and Y. Kobiki, *J. Phys. Chem.* **104**, 1751 (1996).
 - [9] A. Suzuki, M. Yamazaki, Y. Kobiki, and H. Suzuki, *Macromolecules* **30**, 2350 (1997).
 - [10] M. Maaloum, N. Pernodet, and B. Tinland, *Electrophoresis* **19**, 1606 (1998).
 - [11] *D3000 Command Reference Manual* (Digital Instruments, Santa Barbara, CA, 1996).
 - [12] A.-L. Barabási and H. E. Stanley, *Fractal Concepts in Surface Growth* (Cambridge University Press, Cambridge, 1995).
 - [13] H. N. Yang, G. C. Wang, and T. M. Lu, *Diffraction from Rough Surfaces and Dynamic Growth Fronts* (World Scientific, Singapore, 1993).
 - [14] S. J. Fang, S. Haplepete, W. Chen, and C. R. Helms, *J. Appl. Phys.* **82**, 5891 (1997).
 - [15] H. Iwasaki and T. Yoshinobu, *Phys. Rev. B* **48**, 8282 (1993).
 - [16] P. Meakin, *Fractals, Scaling, and Growth far from Equilibrium* (Cambridge University Press, Cambridge, 1998).
 - [17] K. J. Måløy, A. Hansen, E. L. Hinrichsen, and S. Roux, *Phys. Rev. Lett.* **68**, 213 (1992).
 - [18] E. Bouchaud, G. Lapasset, J. Planès, and S. Naveos, *Phys. Rev. B* **48**, 2917 (1993).
 - [19] A. Delaplace, J. Schmittbuhl, and K. J. Måløy, *Phys. Rev. E* **60**, 1337 (1999).
 - [20] S. R. Brown and C. H. Scholz, *J. Geophys. Res.* **90**, 12575 (1985).
 - [21] W. M. Tong, R. S. Williams, A. Yanase, Y. Segawa, and M. S. Anderson, *Phys. Rev. Lett.* **72**, 3374 (1994).
 - [22] G. Porod, in *Small-Angle X-ray Scattering* edited by O. Glatter and O. Kratky (Academic, New York, 1982).
 - [23] G. M. Buendía, S. J. Mitchell, and P. A. Rikvold, in preparation.
 - [24] J. Feder, *Fractals* (Plenum, New York, 1988).
 - [25] A.-L. Barabási and T. Vicsek, *Phys. Rev. A* **44**, 2730 (1991).
 - [26] C. Castelnovo, A. Podestá, P. Piseri, and P. Milani, *Phys. Rev. E*, in press, e-print: cond-mat/0110031.
 - [27] D. Stauffer and A. Aharony, *Introduction to Percolation Theory*, Second Ed. (Taylor & Francis, London, 1992).
 - [28] T. Wårheim and A. Jönsson, *J. Colloid and Interface Sci.* **125**, 627 (1988).
 - [29] G. M. Buendía, S. J. Mitchell, and P. A. Rikvold, in *Computer Simulation Studies in Condensed matter Physics XIV*, edited by D. P. Landau, S. P. Lewis, and H.-B. Schüttler (Springer, Berlin, 2002).
 - [30] B. J. Berne, and R. Pecora, *Dynamic Light Scattering with Applications to Chemistry, Biology, and Physics* (Wiley, New York, 1976).
 - [31] C. S. Johnson and D. A. Johnson, *Laser Light Scattering* (Dover, New York, 1994).

TABLE I: Number of data sets (images) used for analysis.

% Surfactant	Scan Size L [μm]					
	1.25	2.5	5.0	10.0	20.0	Total
0 %	6	5	4	3	2	20
10 %	5	5	5	3	5	23
20 %	5	3	5	5	6	24
30 %	4	5	5	4	2	20
40 %	4	5	4	4	2	19
Grand Total:						106

TABLE II: Summary of results of scaling analysis for templated gel surfaces.

% Surfactant	Roughness Exponent α , from:			RMS Width w_{sat} [nm]	Cross-over length l_{\times} [nm]
	Two-dimensional $\langle w_l \rangle$	One-dimensional $\langle w_l \rangle$	$H_{fast}(r)$		
0 %	0.41 ± 0.02	0.77 ± 0.02	0.63 ± 0.06	1.3 ± 0.1	260 ± 70
10 %	0.56 ± 0.03	0.90 ± 0.02	0.73 ± 0.02	2.3 ± 0.4	260 ± 20
20 %	0.86 ± 0.02	1.009 ± 0.006	0.89 ± 0.02	7.4 ± 0.3	260 ± 10
30 %	0.80 ± 0.01	1.023 ± 0.005	0.87 ± 0.02	41 ± 3	400 ± 40
40 %	0.86 ± 0.02	1.026 ± 0.005	0.83 ± 0.02	80 ± 10	540 ± 30

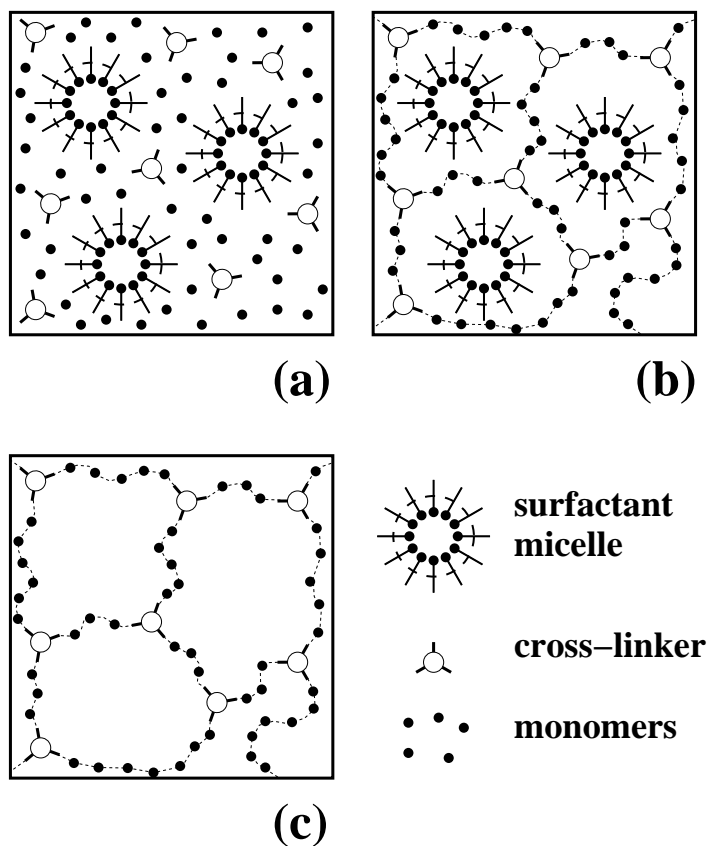


FIG. 1: Schematic representation of templated-gel synthesis. (a) In step one, monomers, cross-linkers, and surfactant micelles are mixed in solution. (b) In step two, polymerization occurs around the unreactive surfactants. (c) In the final step, the surfactants are removed by soaking in distilled water, leaving behind templated voids. The thin dashed lines represent chemical bonds between monomers and cross-linkers. The remaining symbols are explained in the figure legend.

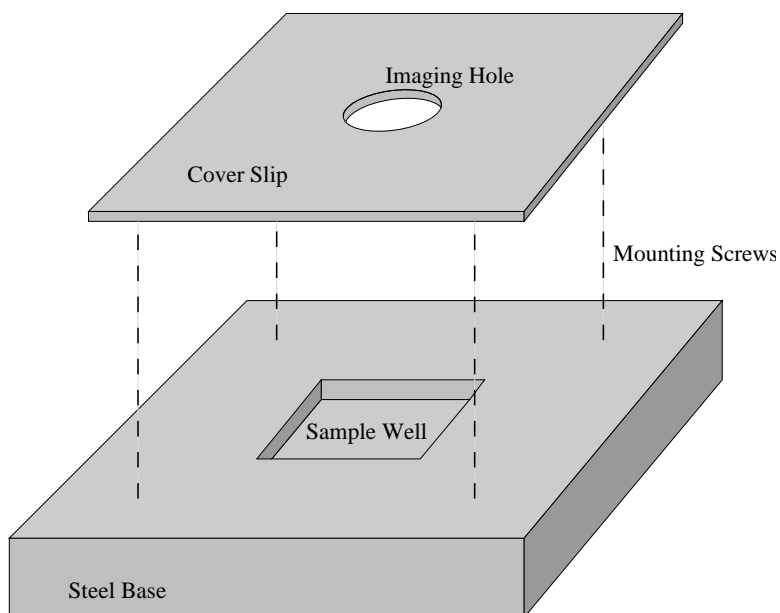


FIG. 2: Schematic representation of the sample holder designed for AFM imaging of hydrogels.

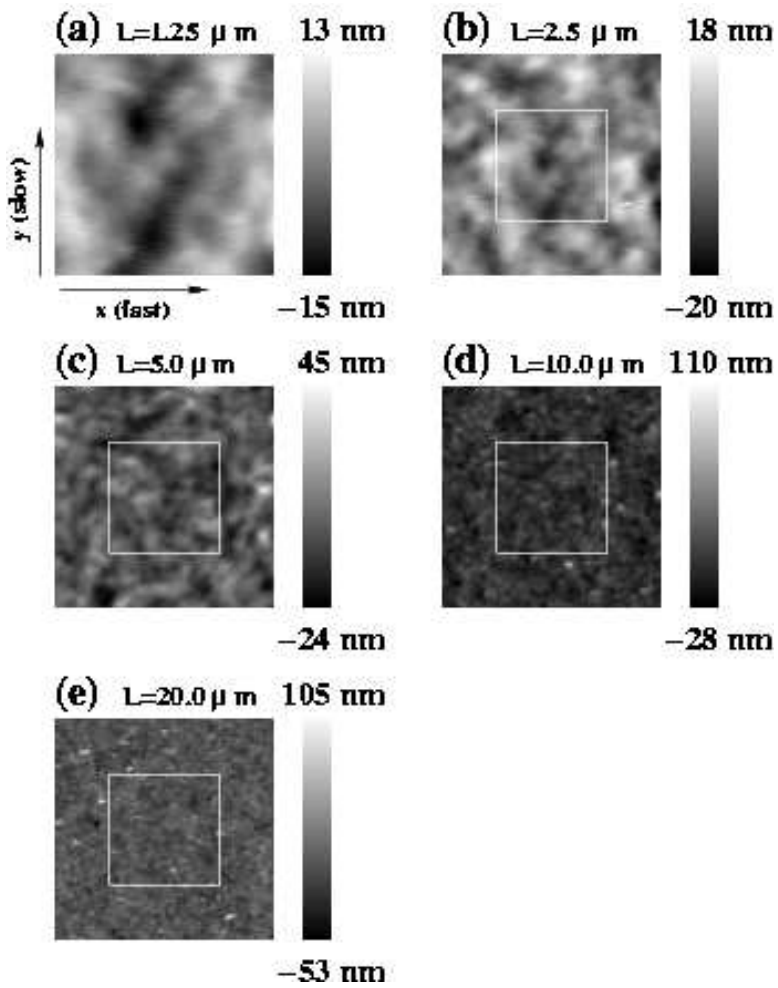


FIG. 3: AFM images of a set of successively zoomed-out images centered at the same location on a 20% templated gel surface. Parts (a) through (e) represent $L \times L$ scan sizes with $L = 1.25, 2.5, 5.0, 10.0,$ and $20.0 \mu\text{m}$, respectively. The gray scale represents the surface height, with white (black) corresponding to the maximum (minimum) height. The lateral drift of the sample was very small. Note the increase in height range with increasing L . The white squares indicate the next smaller scan areas.

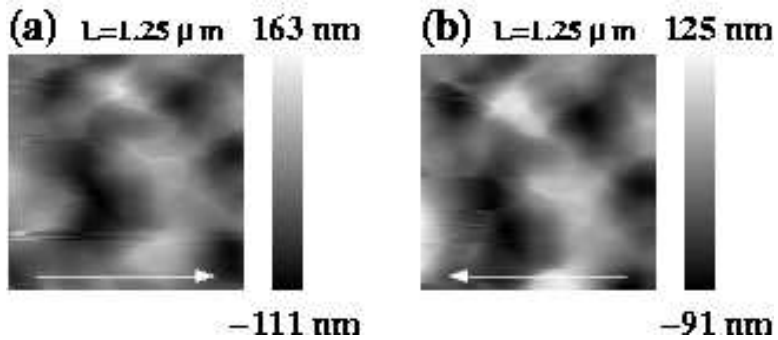


FIG. 4: AFM images of a 40% templated gel surface at $L = 1.25 \mu\text{m}$ scan size, (a) forward scan direction, and (b) reverse scan direction. In each image white (black) corresponds to the maximum (minimum) height. The distortion in the direction of the tip motion (indicated by white arrows) is readily observed.

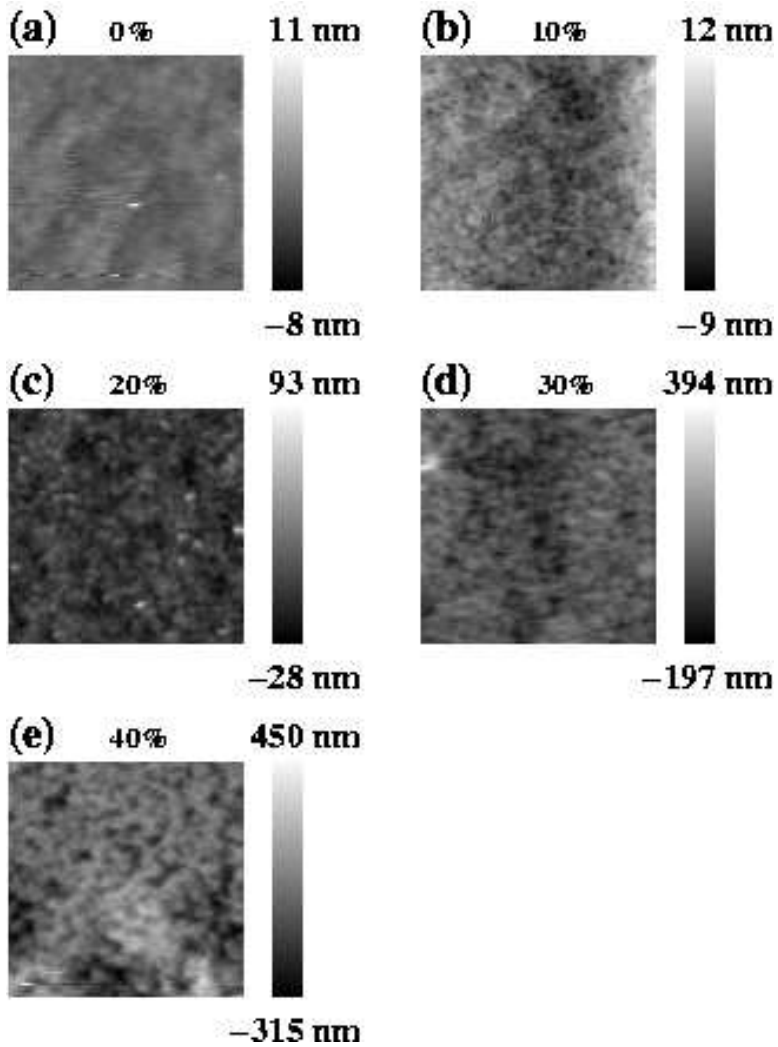


FIG. 5: AFM images of gel surfaces with surfactant concentrations of (a) 0%, (b) 10%, (c) 20%, (d) 30%, and (e) 40%. The scan size is $L = 10.0 \mu\text{m}$ with 512×512 pixel resolution. In each image white (black) corresponds to the maximum (minimum) height. The height range depends strongly on the surfactant concentration, as is also shown in Figs. 6 and 7.

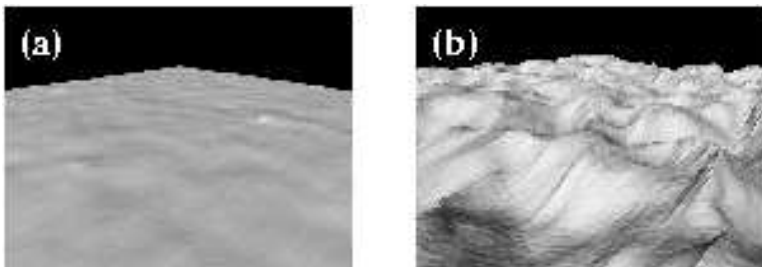


FIG. 6: Three-dimensional views of AFM images of gel surfaces with $L = 10 \mu\text{m}$ and surfactant concentrations of (a) 20%, and (b) 40% (corresponding to Fig. 5 (c) and (e), respectively). The perspective shown is that of an observer sitting at the center of the image at a height of $1 \mu\text{m}$ above the average height of the surface and looking down at a corner. The light source is behind the observer and to the left.

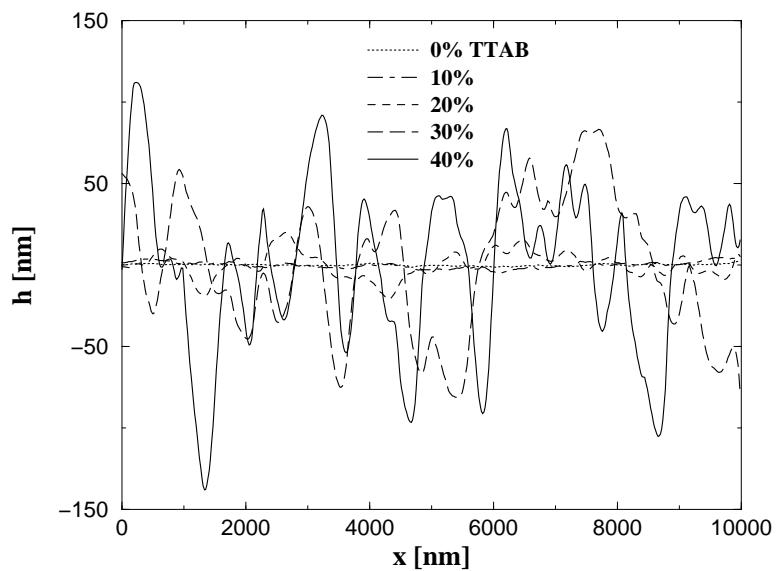


FIG. 7: Plots of typical scan lines for $L = 10.0 \mu\text{m}$ gel surfaces (from Fig. 5) of various surfactant concentrations. Note the strong dependence of the height range on the surfactant concentration.

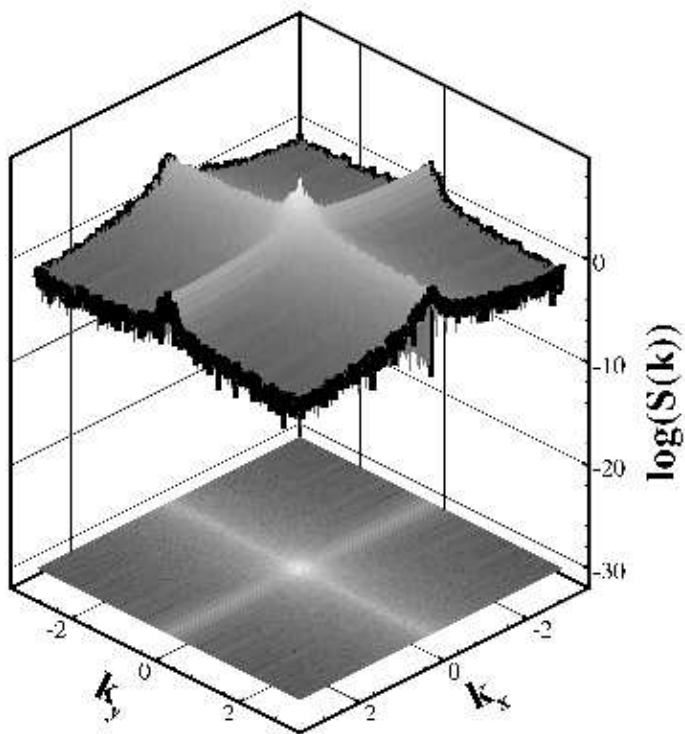


FIG. 8: Structure factor $S(k_x, k_y)$ of a 40% templated gel on a logarithmic gray scale. The structure factor is given in arbitrary units. The anisotropy in the AFM images, which appears as large ridges along the $k_x = 0$ and $k_y = 0$ axes, makes circular averaging unreliable.

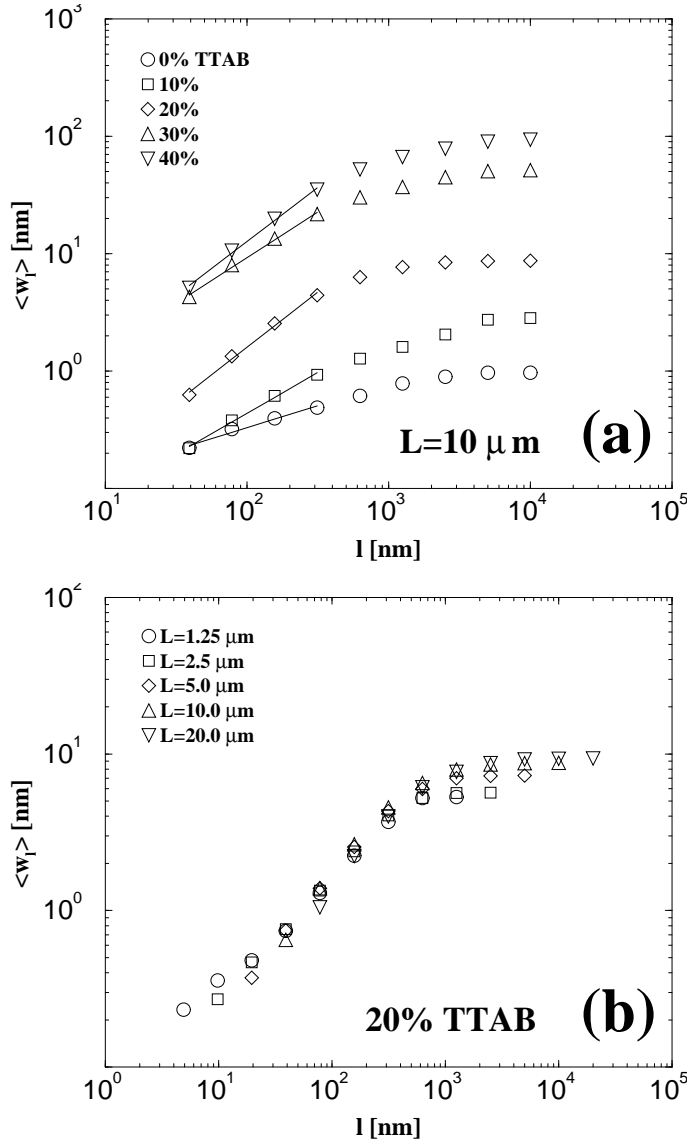


FIG. 9: A typical plot of $\langle w_l \rangle$ vs l on a log-log scale, obtained from two-dimensional images for (a) gel surfaces of various surfactant concentrations (corresponding to Fig. 5) and (b) 20% templated gel surfaces at various scan sizes L (corresponding to Fig. 3). The solid lines in (a) represent linear fits to selected data indicating power-law behavior for limited ranges in l . Note the nice overlap of data for various scan sizes in (b).

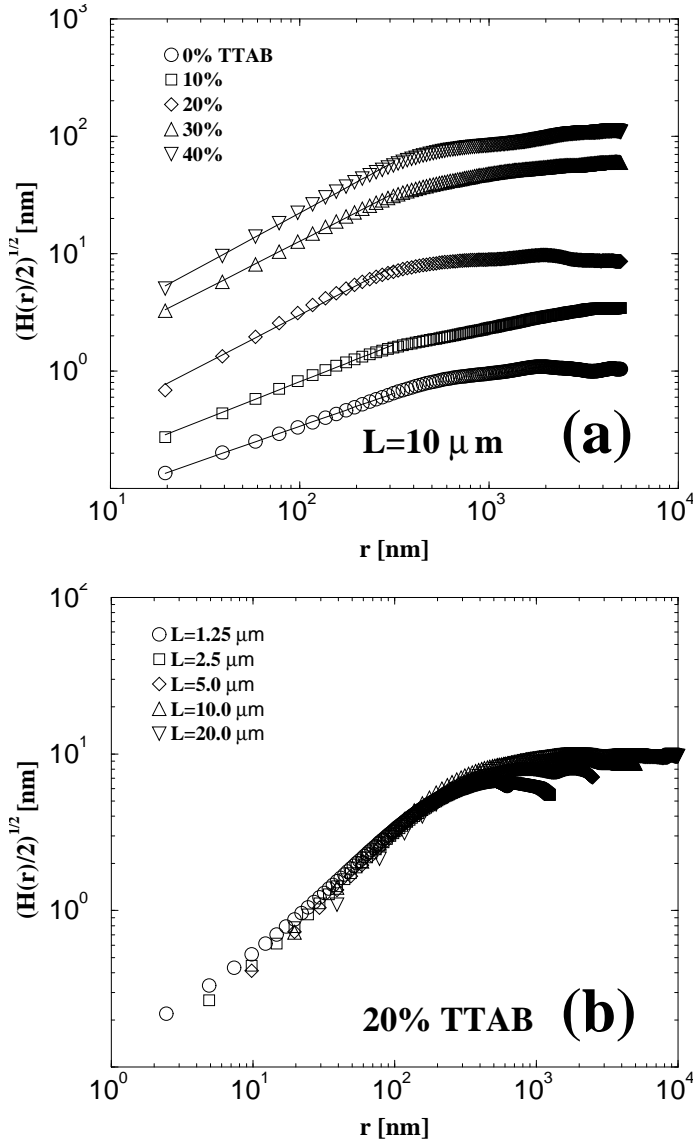


FIG. 10: A typical plot of the one-dimensional $H_{\text{fast}}(r)$ vs r on a log-log scale for (a) gel surfaces of various surfactant concentrations at scan size $L = 10 \mu\text{m}$ (corresponding to Fig. 5) and (b) 20% templated gel surfaces at various scan sizes L (corresponding to Fig. 3). The solid lines in (a) represent linear fits to selected data indicating power-law behavior for limited ranges in r . Note the nice overlap of data for various scan sizes in (b). This figure should be compared with Fig. 9.

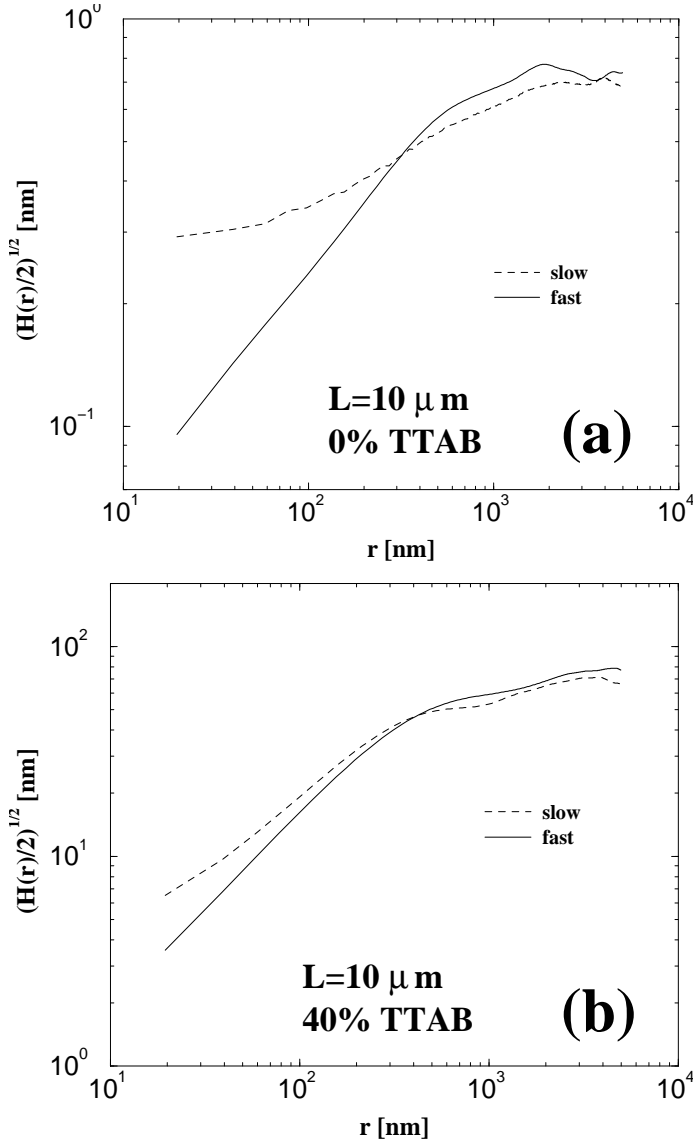


FIG. 11: Plots of the one-dimensional $H_{\text{slow}}(r)$ and $H_{\text{fast}}(r)$ vs r on a log-log scale for $L = 10 \mu\text{m}$ (a) 0% and (b) 40% templated gel surfaces. It is clear that for the untemplated gel surface the signal-to-noise ratio is poor. For the 40% templated gel surface, the noise-induced random offsets between scan lines are smaller, but not negligible.

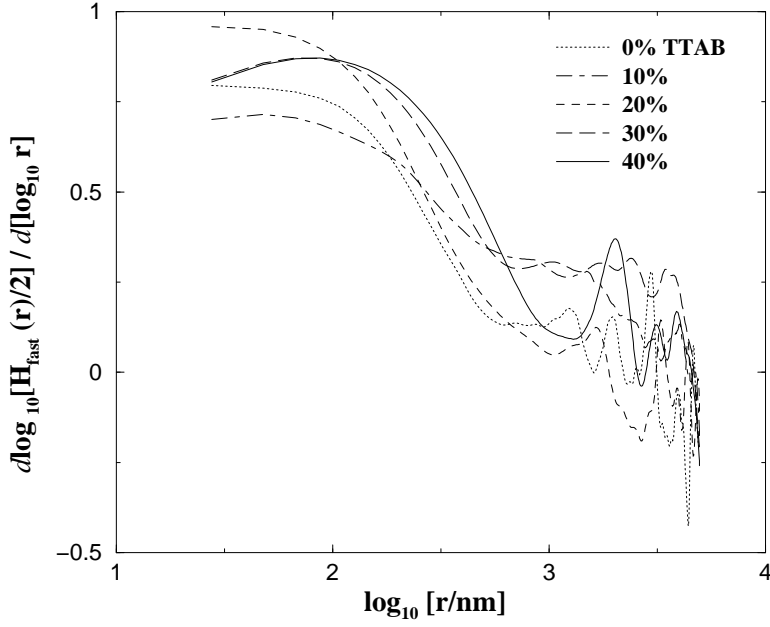


FIG. 12: Plot of $d \log_{10} [H_{\text{fast}}(r)/2] / d[\log_{10} r]$ for $L = 10 \mu\text{m}$. The inflection point of this curve gives an estimate for the lateral cross-over length, l_{\times} , which is listed in Table II.

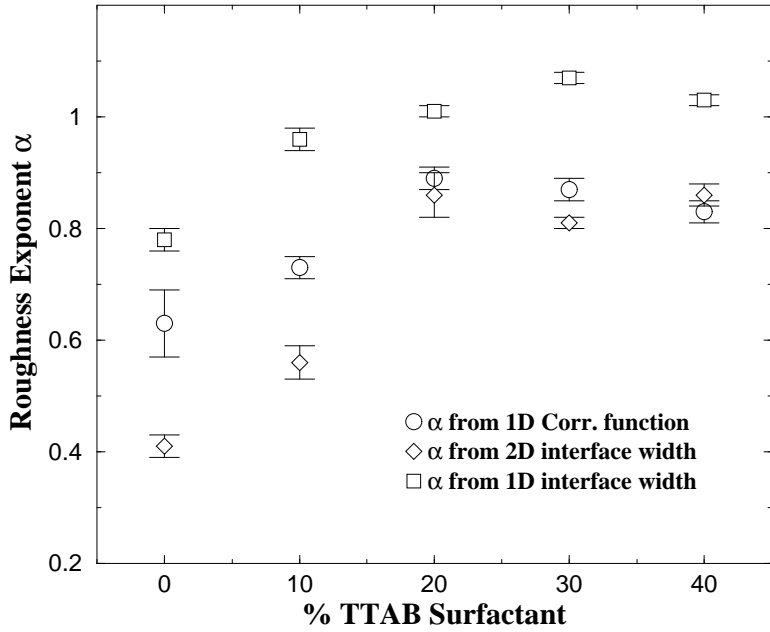


FIG. 13: Roughness exponent α vs surfactant concentration. The measured values of α are averages over the different scan sizes for each surfactant concentration. The error bars represent the standard error.

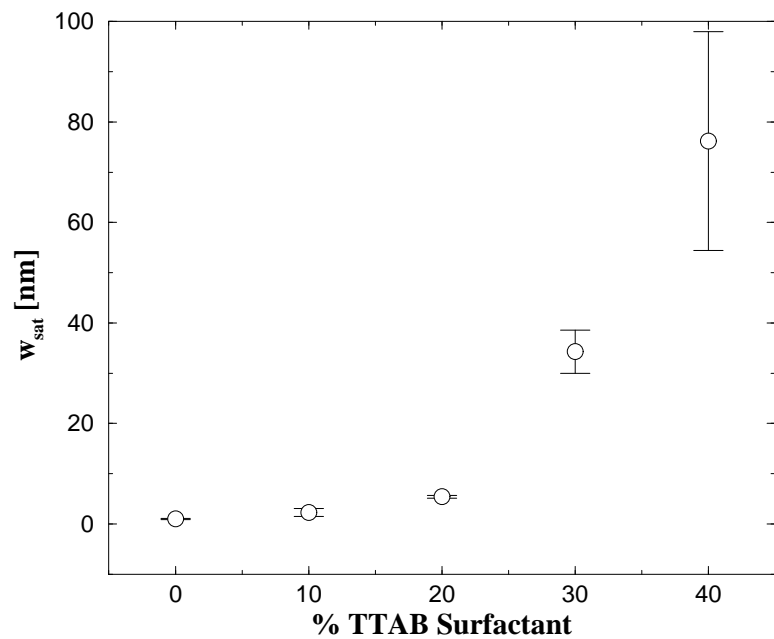


FIG. 14: Saturation surface width w_{sat} vs surfactant concentration. The error bars represent the standard error.

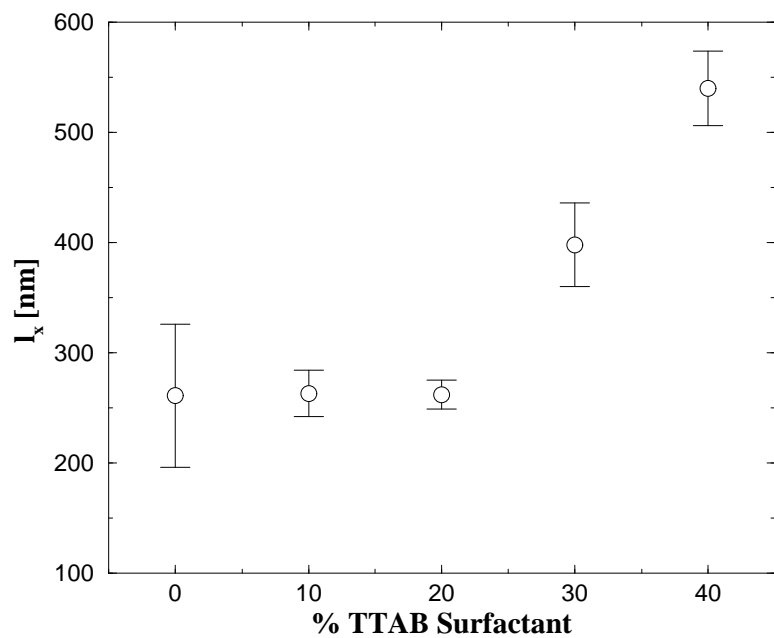


FIG. 15: Cross-over length l_x vs surfactant concentration. The error bars represent the standard error.

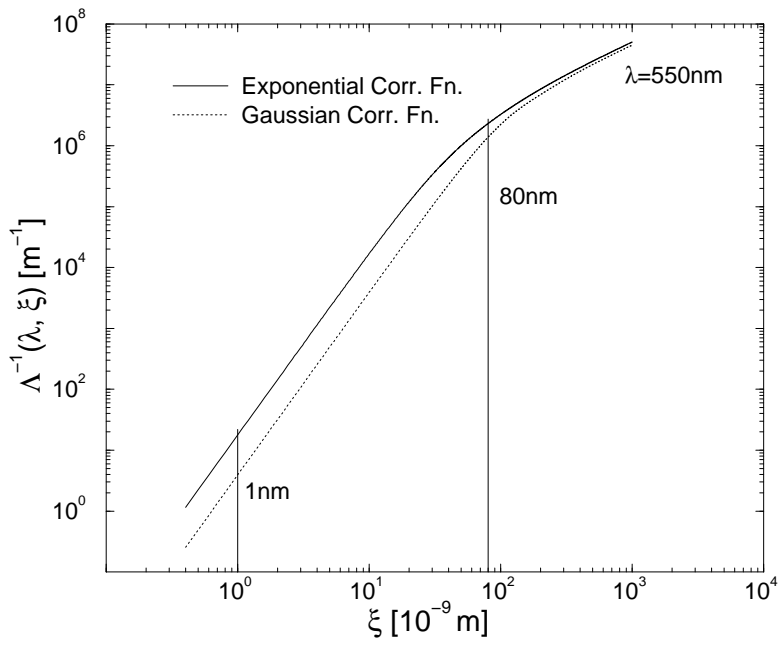


FIG. 16: Turbidity $\Lambda^{-1}(\lambda, \xi)$ vs correlation length ξ for wavelength $\lambda = 550 \text{ nm}$ in the visible region. The solid and dotted curves represent an exponential and a Gaussian form for the correlation function, respectively. Note that the turbidity changes by about six orders of magnitude as the correlation length changes from 1 nm (corresponding to w_{sat} for a 0% templated gel) to 80 nm (corresponding to w_{sat} for a 40% templated gel). This increase in turbidity indicates a change from a transparent to an opaque material.